Geological and Petrological Study on the Debris Avalanche Deposits, Eastern Foot of Zao Volcano, Northeast Japan

Masao Ban *, Fumito Otomo , Motohiro Sato , Takumi Imura

Posted Date: 7 April 2026

doi: 10.20944/preprints202604.0487.v1

Keywords: volcanic edifice collapse; debris avalanche; block facies; matrix facies; volcanic disaster; Zao volcano; Togatta area

 doi:10.20944/preprints202604.0487.v1

Article

Geological and Petrological Study on the Debris Avalanche Deposits, Eastern Foot of Zao Volcano, Northeast Japan

Masao Ban [1,*], Fumito Otomo [1], Motohiro Sato [2] and Takumi Imura [1]

[1] Department of Sciences, Faculty of Science, Yamagata University, 1-4-12, Kojirakawa-machi, Yamagata City, Yamagata, 990-8560, Japan

[2] Volcanic Disaster Prevention Department, Sabo & Landslide Technical Center, Chiyoda-ku, Tokyo 102-0093, Japan; msatores@gmail.com

* Correspondence: ban@sci.kj.yamagata-u.ac.jp; Tel.: +81-23-628-4642

Abstract

Debris avalanche deposits related to the edifice collapse of the summit area of Zao Volcano have been identified for the first time at the volcano's eastern foot. These deposits extend approximately 11–15 km from the summit. Based on their spatial distribution and clast petrology, the deposits are interpreted to have originated from the Umanose caldera. Deposit thickness ranges from 20–30 m in the western and northern parts to over 50 m in the eastern part, with an estimated volume of approximately 0.3 km^3, comparable to that of the summit caldera depression. Matrix facies occur at most outcrops, whereas block facies are found at only three sites. The vertical drop-to-runout distance ratio (H/L) is less than 0.09, which falls within the typical range for debris avalanches but indicates relatively high mobility. Based on its volume and stratigraphic relationships, the collapse is interpreted to have been caused either by a phreatic eruption or by a non-eruptive large-scale failure of a hydrothermally altered zone beneath the summit area. The collapse is considered to mark the onset of the latest activity stage of Zao Volcano, and the petrological characteristics of the magma differ markedly from those of the preceding stage.

Keywords: volcanic edifice collapse; debris avalanche; block facies; matrix facies; volcanic disaster; Zao volcano; Togatta area

1. Introduction

Debris avalanche events caused by volcanic edifice collapse—exemplified by the 1980 eruption of Mount St. Helens (e.g., [1,2]) and the 1888 collapse of Mount Bandai (e.g., [3–5])—have been extensively studied, particularly since the former event. Related studies have revealed that such collapses have occurred at many stratovolcanoes worldwide (e.g., [6,7]). Recent research suggests that volcanic edifice collapse has occurred somewhere in the world more than five times every century [8]. Debris avalanches generated by edifice collapse are typically large-scale and pose a significant volcanic hazard (e.g., [6,7]). In addition, changes in eruptive behavior and magma characteristics before and after edifice collapse have been reported (e.g., [9]), indicating that edifice collapse is also an important factor in reconstructing a volcano's developmental history.

Because such deposits usually occur at the foot of the volcano and are often covered by well-developed vegetation, their presence and distribution are often difficult to determine. As a result, the history of past edifice collapses remains unclear for many active volcanoes. In this study, we focus on Zao Volcano, one of the representative active volcanoes in northeastern Japan, and report the discovery of past debris avalanche deposits. We describe their distribution, facies, and clast characteristics, and discuss the source, mobility, age, and trigger of the debris avalanche.

 doi:10.20944/preprints202604.0487.v1

The Zao Volcano is an active stratovolcano in the central part of the volcanic front of the NE Japan arc (Figure 1). Volcanic activity is divided into six stages, and the most recent stage began at approximately 35 ka (e.g., [10]). The newest stage began with the formation of the Umanose caldera. The formation mechanism of this caldera remains unsolved.

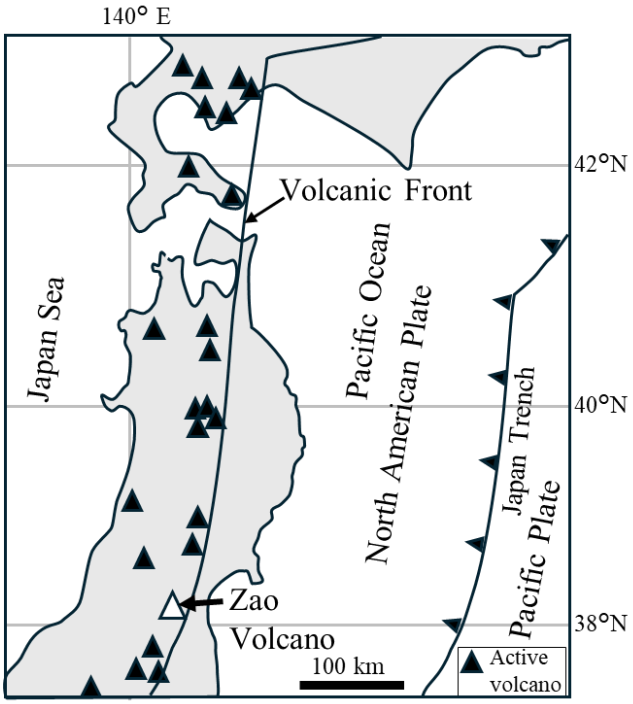

Figure 1. Locality of Zao Volcano.

In the Togatta area, located about 10 km east of Okama—the youngest crater of Zao Volcano—river terraces are developed along the Nigorikawa/Matsukawa River (Figure 2a). Although it had been suggested that the high-level terrace may consist of debris avalanche deposits [11], no detailed investigation had been conducted. In this study, a field investigation of the high-level terrace was carried out, confirming that it is composed of debris avalanche deposits. The source of these deposits was examined by comparing the characteristics of the rock fragments with those of the rocks that constitute the summit caldera. The results obtained in this study will provide useful information for future hazard mitigation, as well as for understanding the eruption history and magma evolution of Zao Volcano.

2. Materials and Methods

Geomorphological and field observations were conducted to determine the distribution of the debris avalanche deposits. The facies of these deposits were described based on field observations.

^{14}C dating was performed on a sample collected from a mudstone below the debris avalanche deposit. The dating was conducted using accelerator mass spectrometry at the High Sensitivity Accelerator Center of Yamagata University. The samples were carefully collected using a stainless steel tool and wrapped in aluminum foil. The samples were chemically cleaned using an acid method before analysis. The calibration of ^{14}C dates was based on IntCal20 [12].

Microscopic observations were carried out on thin sections prepared from 32 selected samples collected from blocks within the deposits. Of these samples used for petrographic analysis, 25 were further selected for whole-rock chemical analysis.

 doi:10.20944/preprints202604.0487.v1

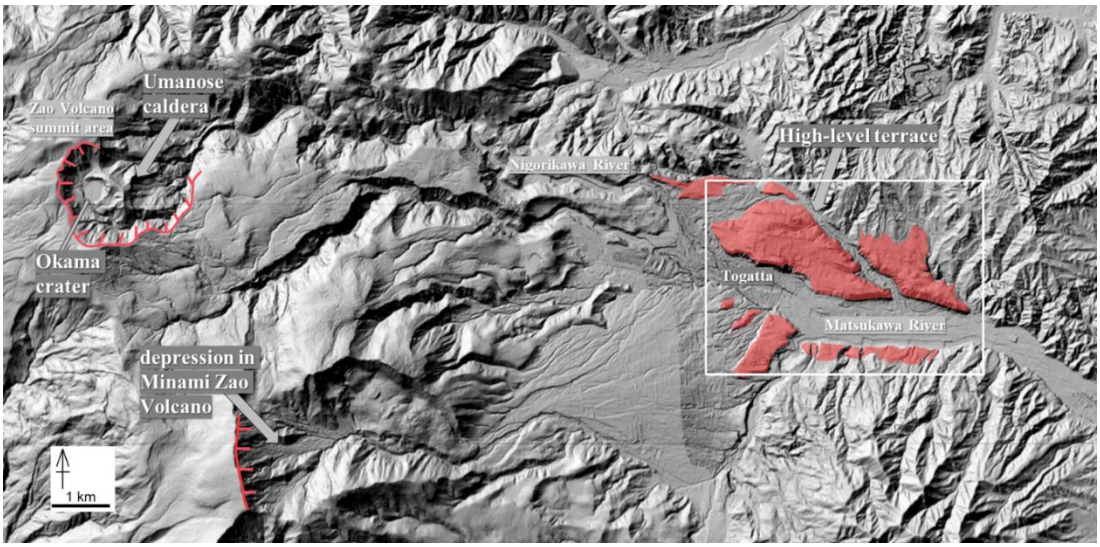

(**a**)

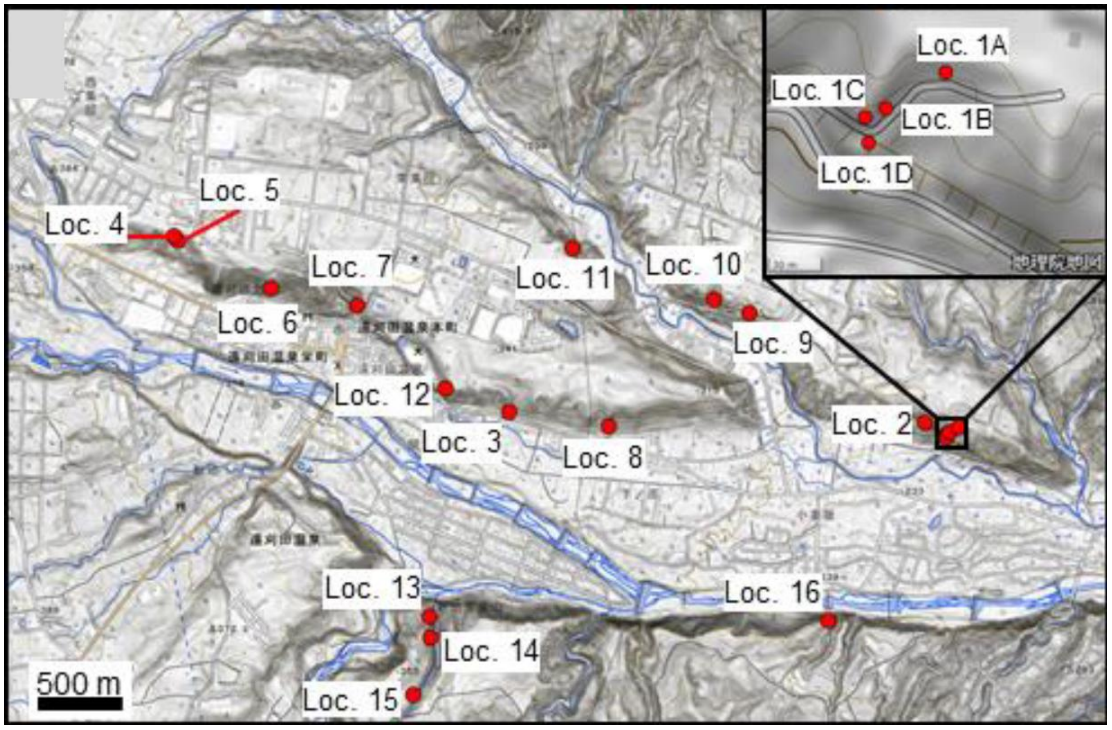

(**b**)

Figure 2. (a) Distribution of the high-level terrace (red colored part). (b) An enlarged map of the square area in (a) showing observation points. The shaded relief map is by the Geospatial Information Authority of Japan.

Whole-rock chemical compositions were analyzed using a wavelength-dispersive X-ray fluorescence spectrometer (ZSX Primus III+, Rigaku) at Yamagata University. Major (Si, Ti, Na, Ca, K, Mg, Fe, Al, Mn, and P) and trace (Ba, Sr, Cr, Ni, V, Rb, Zr, Nb, and Y) elements were determined on glass beads prepared by fusing 1.8 g of powdered sample with 3.6 g of analytical flux (Spectroflux 100B, Johnson Matthey) in a high-frequency bead sampler (NT-2120, Tokyo Kagaku) at 1200 °C, following the method of [13,14]. Analyses were performed under an accelerating voltage of 50 kV and a current of 50 mA. Analytical precision for the trace elements is 5% for Sr, Rb, Zr, Nb, Y, and Ni; 10% for Cr and V; and 5–15% for Ba.

 doi:10.20944/preprints202604.0487.v1

3. Results

3.1. Distribution of Higher Terraces Around the Togatta Area

In the Togatta area, a high-level terrace surface with a relative height of approximately 70–100 m above the Nigorikawa/Matsukawa riverbed can be identified. Its distribution is shown in Figure 2. It is distributed at distances of 10–15 km in a straight line from the summit crater. The remnant terrace surface corresponds to the Togatta Terrace described by [15]. Although [15] examined only the left bank of the Matsukawa River, a terrace of the same level is also distributed on the right bank.

Terrace classification in the Matsukawa drainage basin was first carried out by [16], who, although not illustrating it, divided the terraces—listed from the highest—into the Hara Terrace, the Nagano Terrace, and the Nagafukuro Terrace. The Togatta Terrace is considered to correspond to the Hara Terrace among these. According to [17], this terrace is correlated with the Uemachi Terrace, which is well developed around the Sendai area. As for the age of the Uemachi Terrace, dates of around 40,000 yr BP based on pollen analysis have been reported for the conglomerate layer that forms its main part, and a ^{14}C age of 31,950 ± 3,000 yr BP (ca. 49–31 cal ka BP) has been reported for the overlying peaty silt layer [18,19]. [20] reported an age of 31,500+2,610/−1,970 yr BP (ca. 42–32 cal ka BP) for a wood fragment contained in the conglomerate layer that constitutes the Togatta Terrace.

3.2. Geological Descriptions of the Debris Avalanche Deposits Around the Togatta Area

The debris avalanche deposit comprises the high-level terrace, which is called the Togatta debris avalanche deposit hereafter. Debris avalanche deposits can be divided into block facies, which exhibits depositional features that preserve the original lithological boundaries and structures despite intense fragmentation and deformation, and matrix facies, which is matrix-supported, poorly sorted, and contains a mixture of various clast types (e.g., [21]). The matrix facies sometimes shows heterogeneity; mixing leads to the preservation of original stratigraphy and abrupt facies changes along the deposit, and/or includes clasts showing jigsaw-like structures. In this case, they are also sometimes referred to as mixed facies (e.g., [22]).

Because of dense vegetation, outcrops are difficult to identify in this area except along rivers, which has hindered progress in the investigation. We therefore conducted a thorough survey of the area and, where necessary, removed vegetation using a shovel, enabling us to identify debris avalanche deposits at 11 sites (Figure 2b). Deposits showing the block facies were observed at Locations 1, 2, and 13. At the other locations, the deposits showing mainly matrix facies were observed. The basement rocks were observed at Locations 5, 6, and 7. These are pumice tuff deposits, which would correspond to the Togatta Formation [23]. At Location 11, the debris avalanche deposit covers alteration of sand and mudstones. The presence of sandstone and mudstone interbeds has not yet been documented in this area.

3.2.1. Block Facies

Block facies of the deposit occur at Locations 1, 2, and 13 (Figure 3). At Location 1, the original stratification of several pyroclastic deposit layers is preserved, as illustrated in the figure, although the lower two layers are incompletely mixed (Figure 3a). The outcrop at Location 2 is approximately 20 m high and 30 m wide, and consists of andesite lava with well-developed joints (Figure 3b). The orientations of the joints appear random due to secondary reworking, but they were originally dominated by horizontal and vertical sets. The outcrop at Location 13 is ca. 8 m in width and ca. 5 m in height. The main part consists of light blue to dark brown colored volcanic breccia (Figure 3c). On the right-hand side of the outcrop (Figure 3d), a different heterogeneous volcanic breccia layer, composed of light brown colored and dark brown colored parts, is in contact with the main volcanic breccia. The boundary plane is steep, which suggests the deposits are not primary ones. At the boundary, the volcanic breccias are mixed to some extent.

 doi:10.20944/preprints202604.0487.v1

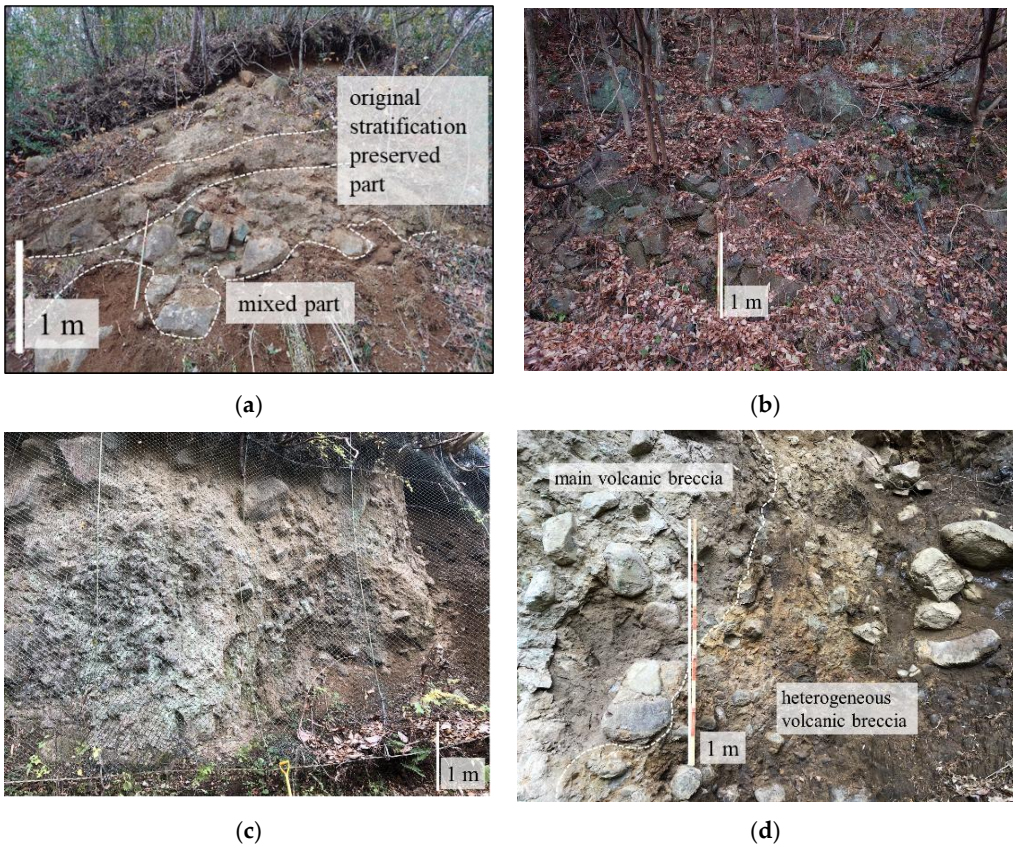

Figure 3. (a) A photograph of the outcrop of the block facies at Location 1C. (b) A photograph of the outcrop of the block facies at Location 2. (c,d) Photographs of the outcrop of the block facies at Location 13. (d) is an enlarged one of the right part of (c).

3.2.2. Matrix Facies

At Locations 3, 4, 5, 8, 9, 10, 11, 12, and 14, the matrix facies were observed. Photographs of the deposits at Locations 4, 8, 9, 12, and 13 are shown in Figure 4. The matrix facies are composed of well-mixed (Figure 4a, c, e) and/or heterogeneous (Figure 4b, d, f, g, h) parts. The heterogeneity of the matrix is evident in a color difference as well as the difference in constituents. The clasts, ranging from a few centimeters to 1.5 m in length, were present. Jigsaw-like cracks are sometimes developed in these clasts (Figure 4c, e).

3.2.3. The Thickness of the Deposit

At Location 5, the basement rocks are exposed at 368 m a.s.l. The elevation of Location 4 is 370 m, and the high-level terrace surface reaches 390 m. Therefore, the thickness of the deposit is approximately 20 m here. At the Localities 6 and 7, the basement rocks were observed at 355 m and 340 m, respectively, and the high-level terrace surface reaches approximately 390 m. Therefore, the thickness of the deposit is less than approximately 35 m here. At Location 11, the boundary between the basement rocks and the debris avalanche deposits is at 300 m a.s.l., and the high-level terrace surface reaches 340 m. Therefore, the thickness of the deposit is approximately 30 m here. At Localities 3 and 8, the debris avalanche deposits are exposed at the base of the higher terrace. Considering that the elevation of the high-level terrace surface in this area is 320–330 m, the thickness of the deposits is estimated to be approximately 40 m. At localities 1, 2, 9, and 10, the lowest elevation of the exposed debris avalanche deposits is 260 m. Considering that the elevation of the high-level terrace surface in this area is approximately 310 m, the thickness of the deposits is estimated to be more than 50 m. Consequently, the deposit is thinner in the western and northern parts (20–30 m) and thicker in the eastern part (>50 m). Based on the estimated thickness of the deposits described

 doi:10.20944/preprints202604.0487.v1

above and the distribution area shown in Figure 2a, the total remnant volume is calculated to be approximately 0.2 km³.

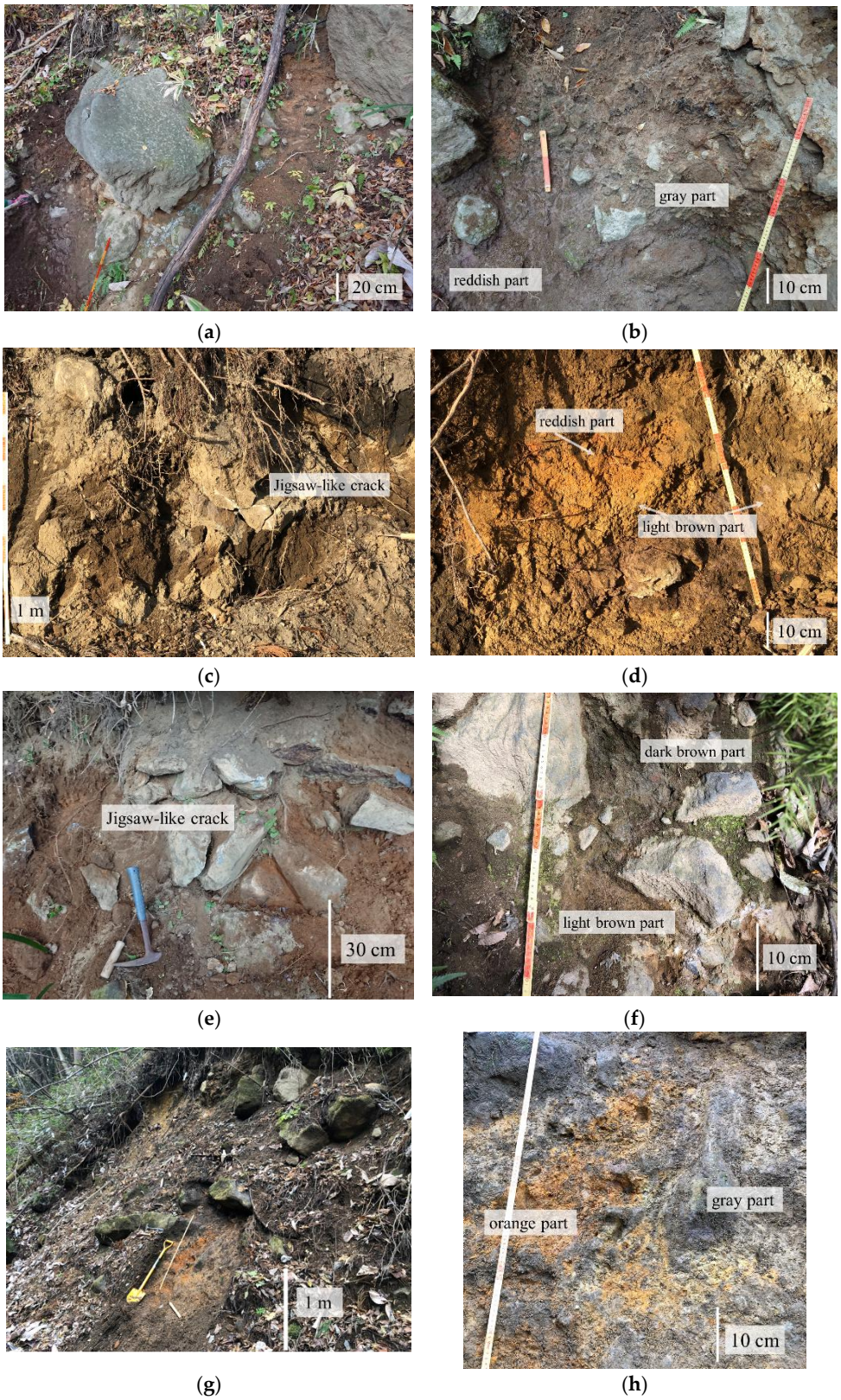

Figure 4. (a,b) Outcrop photographs of the matrix facies at Location 4. (b) is an enlargement of the lower left part of (a). (a) is a well-mixed part, and (b) is a heterogeneous part. (c,d) Photographs of the outcrop of the matrix facies at Location 8. (c) is a well-mixed part, and (d) is a heterogeneous part. A jigsaw-like crack in a clast (central part) is observed in (c). (e) A photograph of the outcrop of the matrix facies at Location 10, including a small block showing a jigsaw-like crack (central part) in a well-mixed matrix. (f) A photograph of the outcrop of the

 doi:10.20944/preprints202604.0487.v1

matrix facies at Location 10, showing a heterogeneous matrix observed in a color difference. (g,h) Photographs of the outcrop of the matrix facies at Location 14. (h) is an enlargement of the lower middle part of (g), showing a heterogeneous matrix observed in a color difference.

3.3. The Result of ^{14}C Dating

The sample collected from the mudstone (Figure 5) beneath the debris avalanche deposit at Location 11 was dated by the ^{14}C method. The result is presented in Table 1. The result shows an average calibration age of 43 ka.

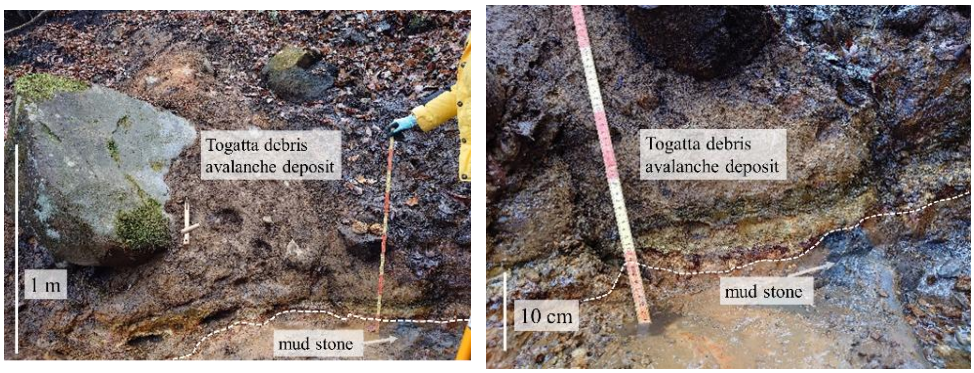

(**a**) (**b**)

Figure 5. (a) A photograph of a mudstone beneath a debris avalanche deposit at Location 11. (b) Close-up of the basal part of (a).

Table 1. Result of ^{14}C age dating.

Location	Sample	$\delta^{13}C$ (‰)	^{14}C age (yrsBP±1σ)	Calibration age (relative probability, 1σ)	Calibration age (relative probability, 2σ)	Average of calibration age (2σ) (ka)
11	mudstone	-28.72±0.22	39627±248	41082 BCE (68.3%) 40803 BCE	41281 BCE (95.4%) 40657 BCE	43

The sample was prepared by acid washing.

3.4. Rock Type and Whole Rock Compositions of the Clasts in the Debris Avalanche Deposit

Whole-rock compositions of representative clasts are presented in Table 2. The variation diagrams are presented in Figures 6 and 7. SiO_2 contents of the clasts are 55-65 wt.%. The clasts can be divided into the following four types: (1) medium-K calc-alkaline series two-pyroxene basaltic andesite to dacite, (2) medium-K calc-alkaline series quartz-olivine-bearing two-pyroxene basaltic andesite to andesite, (3) medium-K tholeiitic series quartz-olivine-bearing two-pyroxene basaltic andesite, and (4) low- to medium-K tholeiitic series two-pyroxene basaltic andesite to andesite. Type (1) is predominant, followed by Type (2). Types (3) and (4) are rarely observed.

In general, K_2O, Na_2O, Rb, Ba, Zr, Y, and Nb contents increase, whereas TiO_2, Al_2O_3, CaO, MgO, Sr, V, and Ni contents decrease with increasing SiO_2 content. The data show moderate scatter in the Cr plot. Two tholeiitic rocks are plotted in the low-K series region (Figure 6). These two samples are plotted on the lower part of the Rb diagram (Figure 7).

Table 3. Major and trace element chemical compositions of the clasts from the Togatta debris avalanche deposit.

(wt%)	SiO_2	TiO_2	Al_2O_3	FeO*	MnO	MgO	CaO	Na_2O	K_2O	P_2O_5	FeO*/MgO
Type: CA two px BA to Dac											
20211125_1A-2	61.03	0.79	16.19	7.91	0.14	3.08	6.53	2.94	1.27	0.12	2.56
20211125_1C-1	61.29	0.77	15.77	8.08	0.12	3.29	6.18	2.9	1.45	0.14	2.45
20211125_1C-3	63.89	0.73	15.84	7.07	0.12	2.72	4.9	2.97	1.68	0.09	2.6

 doi:10.20944/preprints202604.0487.v1

20211125_3-3	60.86	0.8	16.2	7.71	0.13	3.18	6.87	2.81	1.33	0.12	2.43
20211125_3-4	63.58	0.7	15.62	6.93	0.12	2.66	5.56	3.06	1.67	0.11	2.61
20211125_3-7	60.26	0.76	16.23	8.37	0.13	3.41	6.51	2.87	1.32	0.13	2.45
20211100_1C-1	62.09	0.72	15.51	7.55	0.12	3.08	6.23	3.03	1.53	0.12	2.45
20221128_3-scoria	58.26	0.75	16.68	7.78	0.15	4.88	7.76	2.67	0.98	0.09	1.59
20221108_4WH-1	63.06	0.72	15.63	6.73	0.11	2.79	6.11	3.11	1.62	0.12	2.41
20221128_8A-3	64.44	0.73	15.86	6.89	0.11	2.62	4.59	2.92	1.72	0.11	2.63
20221128_8B-2	65.37	0.75	16.16	6.53	0.12	2.57	3.85	2.75	1.81	0.11	2.54
20221111_9-1	61.87	0.83	16.72	7.91	0.13	3.28	5.52	2.53	1.1	0.12	2.41
20221111_9-2	61.32	0.79	16.53	8.03	0.13	3.33	5.97	2.65	1.12	0.12	2.41
20231203_11-L1	58.24	0.89	16.79	8.07	0.16	4.01	7.77	2.87	1.07	0.14	2.01
20231203_11-L2	57.32	0.93	16.87	8.57	0.16	3.97	8.02	2.91	1.09	0.16	2.16
20231203_11-L4	58.9	0.86	16.85	8.23	0.14	3.3	7.77	2.86	0.99	0.1	2.49
20231203_11-U1	59.34	0.85	16.57	8.23	0.14	3.77	6.93	2.85	1.18	0.14	2.19
20231203_11-U2	59.52	0.85	16.49	8.01	0.14	3.75	7.01	2.92	1.18	0.14	2.13
20231203_11-U3	57.75	0.94	18.47	8.34	0.15	4.3	6.09	2.59	1.16	0.19	1.94
20231203_11-U6	60.99	0.78	16.13	7.65	0.14	3.55	6.46	2.85	1.33	0.11	2.16
20231123_14-1	63.31	0.72	15.97	6.39	0.11	2.87	6.15	3.01	1.36	0.1	2.23
20231123_14-2	62.41	0.76	16.72	6.44	0.1	3	6.22	2.83	1.41	0.1	2.14
20231123_14-7	60.95	0.79	16.45	8.24	0.13	3.22	6.07	2.81	1.22	0.12	2.56
20231123_14-8	65.15	0.83	16.66	7.53	0.1	2.37	3.31	2.33	1.6	0.12	3.17
20231203_12-3	56.37	0.94	17.95	8.42	0.15	4.22	7.88	2.89	0.97	0.2	1.99
Type: CA qtz-olv b.g. two px BA											
20221108_5-1	57.1	0.97	18.04	8.22	0.15	3.85	7.55	2.88	1.03	0.21	2.13
20221108_10-3	57.54	0.83	16.98	8.13	0.15	4.8	7.52	2.79	1.1	0.14	1.69
20231123_14-4	56.71	0.89	17.34	8.4	0.15	4.23	8.18	2.9	1.01	0.2	1.98
Type: TH qtz-olv b.g. two px BA											
20211125_1A-1	56.69	0.9	17.1	9.01	0.15	3.83	8.13	2.93	1.06	0.2	2.35
20211125_3-1	56.05	0.9	17.03	9.96	0.15	4.06	7.76	2.86	1.02	0.21	2.45
20211125_3-2	57.17	0.9	17.19	8.85	0.15	3.7	7.83	2.91	1.1	0.2	2.39
Type: TH two px BA to And											
20231203_11-U8	55.02	1.09	19.69	9.42	0.17	4.63	6.81	2.5	0.54	0.14	2.03
20231203_12-1	55.17	0.92	18.18	8.12	0.15	4.16	9.32	2.74	1.06	0.18	1.95
20231203_11-U4	58.47	0.99	16.12	10.04	0.14	3.31	7.35	2.89	0.49	0.19	3.03
(ppm)	Rb	Ba	Sr	Y	Zr	Nb	Cr	Ni	V	Cu	Zn
Type: CA two px BA to Dac											
20211125_1A-2	35.3	400	246	26.3	113	4.2	26.2	12.6	163	27.7	66.9
20211125_1C-1	40.5	411	264	30.9	123	4.5	39.9	19.4	169	21.6	66.1
20211125_1C-3	48.2	464	219	26	137	5.3	54.1	13.6	178	24.2	65.2
20211125_3-3	30.5	359	258	28.9	117	5.1	50	11.4	186	26.4	94.9
20211125_3-4	43.7	480	249	29.4	137	5.3	33.1	13.3	164	20.7	60.1
20211125_3-7	35.6	403	280	26.3	115	4.6	31.9	19.9	141	23.8	70.9
20211100_1C-1	41.7	403	258	28.6	128	5.3	46.6	15.8	151	21	65.2
20221128_3-scoria	26.1	316	261	22.7	97	3.9	42.6	47.7	149	20.9	67.9
20221108_4WH-1	43.2	446	258	29.4	129	5.1	99	12.2	170	19.3	57.7
20221128_8A-3	46.6	480	219	30.4	142	5.8	54.1	11.7	198	21.9	65.5
20221128_8B-2	51.3	499	206	32.5	149	5.7	30.4	11.9	137	28.6	66.7
20221111_9-1	31.4	413	238	24.6	122	5.4	25.1	12.7	133	20.1	100.2
20221111_9-2	31.1	385	249	25.2	116	4.5	31.3	13	161	22.2	96.4
20231203_11-L1	27.7	331	289	24.7	102	5.3	73.5	16.7	182	23.8	69.6
20231203_11-L2	27.5	345	320	26.2	101	4.2	61.6	15.9	183	34.3	71.9
20231203_11-L4	25.3	314	262	26.1	94	3.6	49.7	8.1	188	12.1	66.1
20231203_11-U1	31.1	357	269	24.4	102	4.6	33.3	18.3	163	28.8	72

 doi:10.20944/preprints202604.0487.v1

20231203_11-U2	30.7	350	267	25.3	101	4.8	45.9	15	193	32.3	68.3
20231203_11-U3	23.1	450	328	30.6	114	5.3	49.9	26	183	23.2	76.5
20231203_11-U6	30.8	381	237	26.4	115	4.7	47.2	13.1	182	27.4	69.6
20231123_14-1	35.2	359	228	42.7	116	4.4	64.1	9.6	229	17.8	97.8
20231123_14-2	36.6	368	245	39.4	118	4.6	62.3	18.2	122	33.4	55.2
20231123_14-7	28	380	240	32.5	111	4.8	29.4	17.8	163	23.3	85
20231123_14-8	51.5	748	269	26.2	158	5.5	61.2	11.5	185	41.4	51.3
20231203_12-3	25.9	377	376	30.1	119	5.1	75.8	23	213	26.1	76.1
Type: CA qtz-olv b.g. two px BA											
20221108_5-1	18.2	446	371	26.1	116	6.2	37.6	23.3	141	19.7	75.4
20221108_10-3	27.5	375	313	25.8	108	4	34.9	34.9	165	23.8	69.4
20231123_14-4	23.6	328	367	26.5	104	5.1	47.3	24.8	197	31.8	73.3
Type: TH qtz-olv b.g. two px BA											
20211125_1A-1	26.6	342	369	25.2	108	5.3	50.8	17.4	191	24.4	69.7
20211125_3-1	25.6	364	370	29.2	107	5.3	33.5	26.5	125	17.2	69.7
20211125_3-2	29.1	357	368	24.5	111	4.5	48	22.8	186	37.6	69.5
Type: TH two px BA to And											
20231203_11-U8	12.3	470	314	27.3	125	5.4	35.5	22.4	229	15.3	89.2
20231203_12-1	32	342	383	33.7	94	3.6	29.4	11.7	163	40.9	71.1
20231203_11-U4	8.6	214	244	32.5	82	4.6	45.6	3.6	181	27.3	94.4

CA, calc-alkaline; TH, tholeiite; BA, basaltic andesite; And, andesite; Dac, dacite; px, pyroxene; qtz, quartz; olv, olivine; FeO*, total iron calculated as FeO. All oxide values are normalized to 100%.

 doi:10.20944/preprints202604.0487.v1

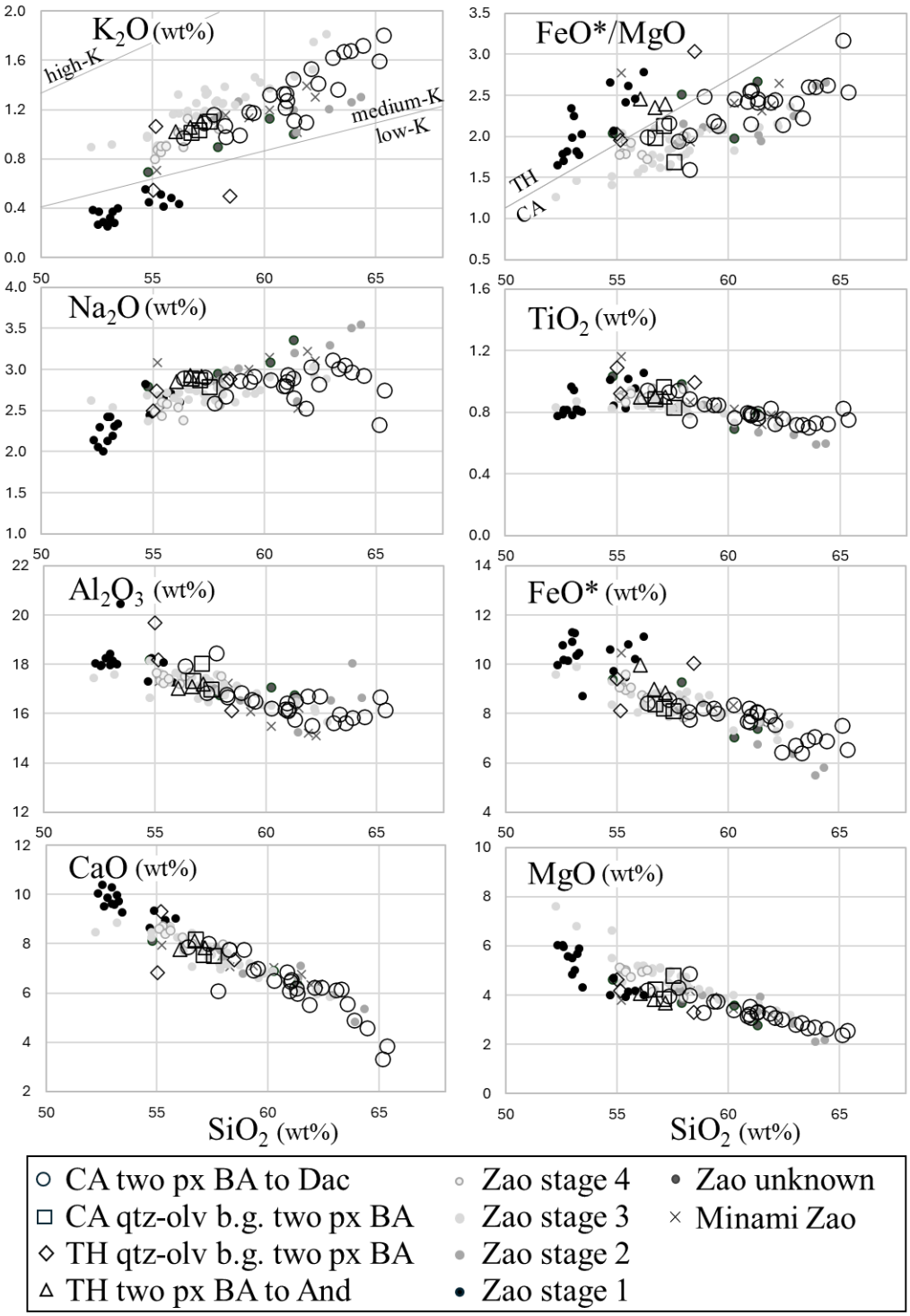

Figure 6. Major element SiO_2 variation diagrams of the clasts in the Togatta debris avalanche deposits. The rock data from the Zao Volcano [24,25] and the Minami Zao Volcano [26] are also plotted. The boundary lines in the K_2O vs. SiO_2 and FeO*/MgO vs. SiO_2 diagrams are from [27] and [28], respectively. TH, tholeiite; CA, calc-alkaline; BA, basaltic andesite; And, andesite; Dac, dacite; px, pyroxene; qtz, quartz; olv, olivine; FeO*, total iron calculated as FeO.

 doi:10.20944/preprints202604.0487.v1

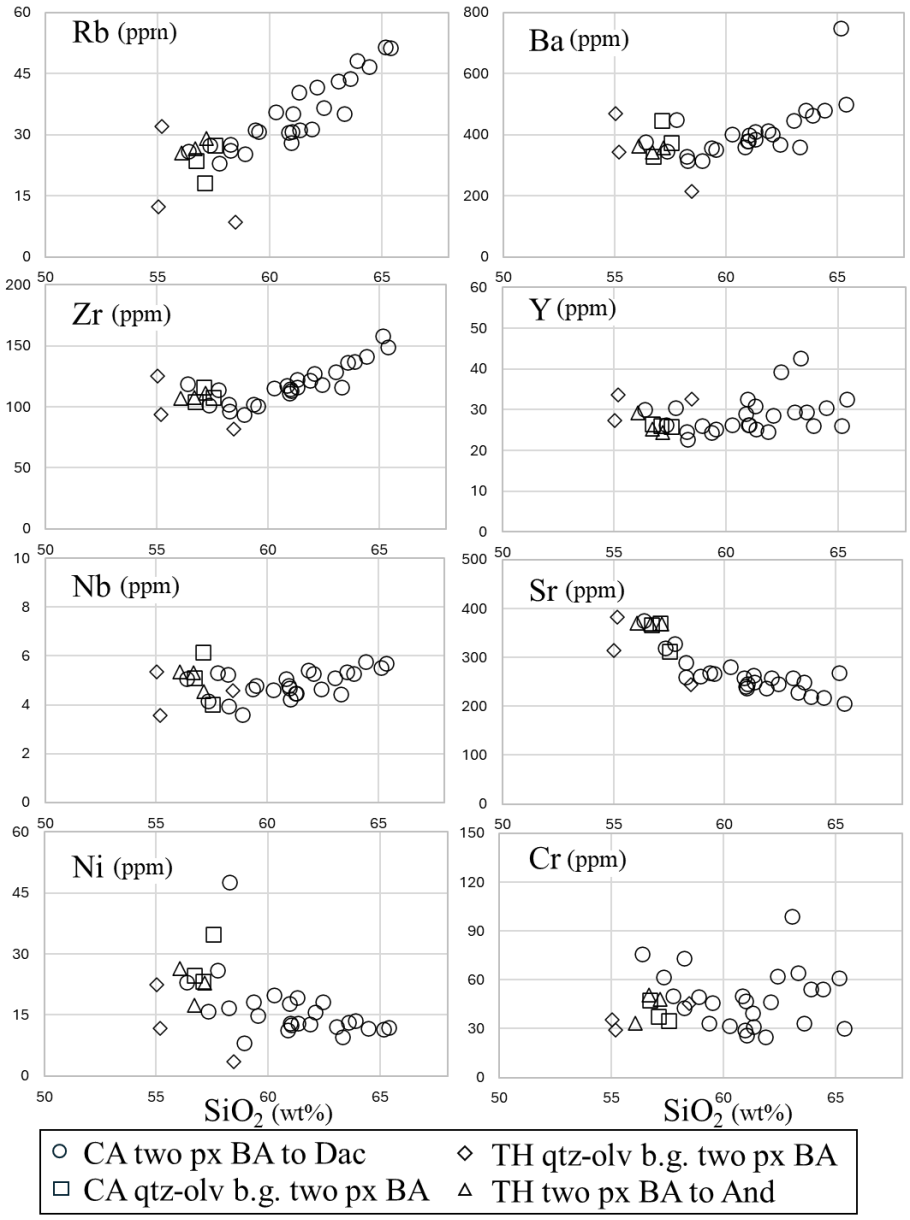

Figure 7. Trace element SiO_2 variation diagrams of the clasts in the Togatta debris avalanche deposits. TH, tholeiite; CA, calc-alkaline; BA, basaltic andesite; And, andesite; Dac, dacite; px, pyroxene; qtz, quartz; olv, olivine.

3.5. Petrographic Characteristics of the Clasts in the Debris Avalanche Deposit

The petrographic characteristics of calc-alkaline two-pyroxene basaltic andesite to dacite, calc-alkaline quartz-olivine-bearing two-pyroxene basaltic andesite, tholeiitic two-pyroxene basaltic andesite to andesite, tholeiitic quartz-olivine-bearing two-pyroxene basaltic andesite, are described below. The photomicroscope images of the representative samples are shown in Figure 8.

3.5.1. Calc-Alkaline Series Two-Pyroxene Basaltic Andesite to Dacite

This type has phenocrystic plagioclase (up to 4.5 mm), orthopyroxene (up to 1.2 mm), clinopyroxene (up to 2.2 mm), and opaque minerals (up to 0.6 mm) in a hyalo-ophitic-textured groundmass (Figure 8a–b). The phenocrysts mostly show subhedral. More than half of the plagioclase grains exhibit dissolution textures, such as honeycomb, dusty, and patchy textures, whereas the others do not. Orthopyroxene phenocrysts are without a reaction rim of clinopyroxene. The glomerocrysts, composed of plagioclases, pyroxenes, and opaque minerals, are occasionally observed.

 doi:10.20944/preprints202604.0487.v1

3.5.2. Calc-Alkaline Series Quartz-Olivine-Bearing Two-Pyroxene Basaltic Andesite

This type contains phenocrystic plagioclase, two pyroxenes, and opaque minerals with minor amounts of phenocrystic olivine and quartz in an intersertal-textured groundmass (Figure 8c). Plagioclase (up to 2.5 mm), orthopyroxene (up to 1.3 mm), clinopyroxene (up to 2.0 mm), olivine (up to 0.8 mm) phenocrysts mostly show euhedral to subhedral, whereas quartz phenocryst (up to 1.2 mm) and the opaque minerals (up to 0.6 mm) show anhedral to subhedral. Approximately half of the plagioclase phenocrysts exhibit dissolution textures. Orthopyroxene phenocrysts do not have clinopyroxene reaction rims. Olivine phenocrysts sometimes have a thin reaction rim of pyroxenes.

3.5.3. Tholeiitic Quartz-Olivine-Bearing Two-Pyroxene Basaltic Andesite

This type shares petrographic characteristics with the calc-alkaline quartz-olivine-bearing two-pyroxene basaltic andesite.

3.5.4. Tholeiitic Basaltic Andesite to Andesite

This type contains phenocrystic plagioclase (up to 3.2 mm), orthopyroxene (up to 1.1 mm), and clinopyroxene (up to 1.2 mm) in an intersertal-textured groundmass (Figure 8d). The phenocrysts mostly show euhedral to subhedral. Approximately half to one-third of the plagioclase phenocrysts exhibit the dissolution texture, whereas the others do not.

This type includes low and medium-K. The medium-K rocks rarely include basaltic groundmass [29] and glomerocrysts composed of plagioclases, pyroxenes, and opaque minerals, which are not observed in the low-K rocks. Whereas the low-K rocks include orthopyroxene phenocrysts having clinopyroxene reaction rims, which are not included in the medium-K rocks. Pyroxene phenocrysts in the low-K rocks are relatively scarce compared to the medium-K rocks.

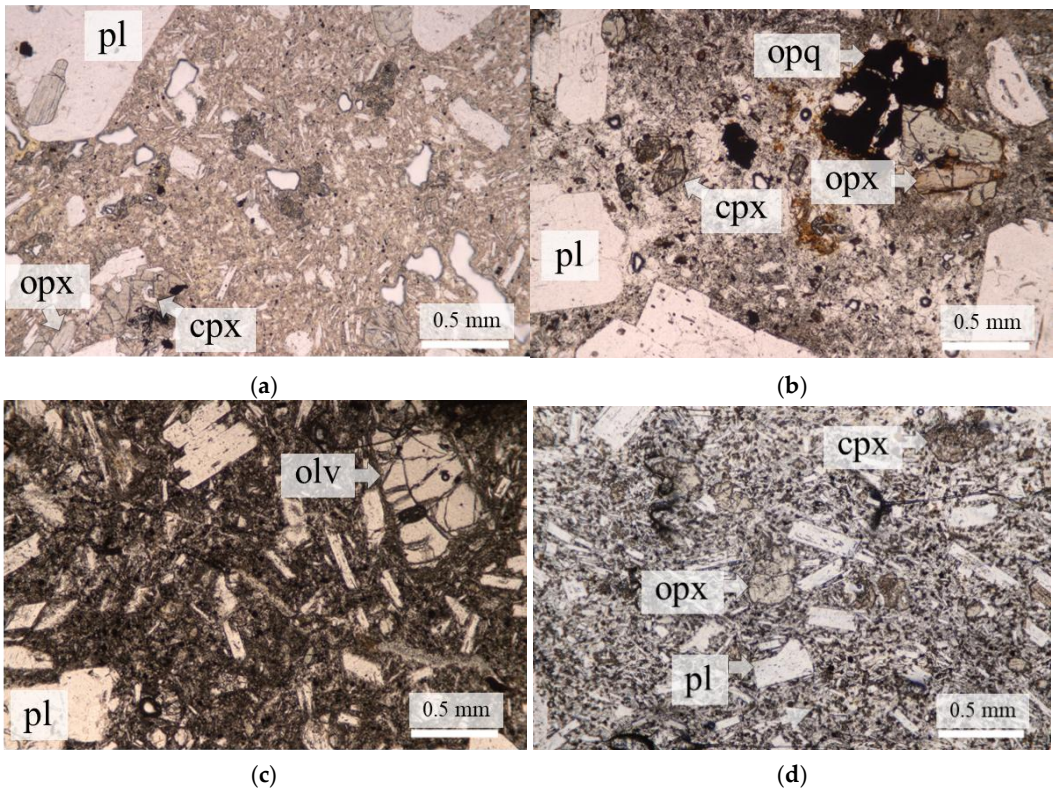

Figure 8. Photomicroscope images of the clasts in the Togatta debris avalanche deposits. (a) Calc-alkaline two-pyroxene andesite, (b) Calc-alkaline two-pyroxene dacite, (c) Calc-alkaline quartz-olivine-bearing two-pyroxene basaltic andesite, and (d) Tholeiitic two-pyroxene basaltic andesite. Plg, plagioclase; px, pyroxene; qtz, quartz; olv, olivine, opq, opaque mineral.

 doi:10.20944/preprints202604.0487.v1

4. Discussion

4.1. Source Area of the Togatta Debris Avalanche Deposit

As described in the Results section, the debris avalanche deposit was recognized for the first time at the eastern foot of Zao Volcano. This deposit is distributed along the Nigorikawa/Matsukawa River, which originates from the summit area of Zao Volcano (Figure 2a). Therefore, it likely formed as a result of a summit collapse that formed the Umanose caldera. To further confirm this interpretation, the rock types of the clasts within the deposit were compared with those of the volcanic edifice. The chemical compositions of products forming the Zao volcanic edifice are plotted using the stage classification of [24]. Although the stages defined in [24] were later revised into six stages by [10], the classification of [24] is adopted here because it provides a larger dataset. The stages 1, 2, 3, and 4 of [24] approximately correspond to stages 1, 2–3, 4–5, and 6 of [10], respectively. In addition, data from [25], which reported further analyses of products from stages 1 and 3 of [24], are also included. All rocks, except those from the most recent stage, potentially occur in the Umanose caldera.

The oldest stage (Stage 1 in [24]) rocks of Zao Volcano belong to the low-K tholeiitic series, whereas rocks from the younger stages (Stages 2–4 in [24]) belong to the medium-K calc-alkaline series. As described in the Results section, most clasts in the debris avalanche deposit belong to the medium-K calc-alkaline series, including Type (1) two-pyroxene basaltic andesite to dacite and Type (2) quartz-olivine-bearing two-pyroxene basaltic andesite to andesite. In contrast, the two minor types (Types (3) and (4)) belong to the tholeiitic series.

The whole-rock compositions of the medium-K calc-alkaline clasts fall within the compositional range of medium-K calc-alkaline rocks of Zao Volcano. Among the tholeiitic clasts, the low-K tholeiitic type two samples plot within or along the extension of the trends defined by Stage 1 rocks of Zao Volcano; however, the medium-K tholeiitic clasts have not been reported from rocks composing Zao Volcano.

Moreover, such medium-K tholeiitic rocks have not been reported from volcanoes along the volcanic front of the Northeast Japan arc north of Nasu Volcano (e.g., [30]). In addition, Type (3) clasts exhibit disequilibrium petrographic features that have not been described in tholeiitic rocks from volcanoes in Northeast Japan. The origin of the medium-K tholeiitic clasts remains unclear, and they are treated here as rare and exceptional components.

Based on the above considerations, it is reasonable to conclude that the Umanose caldera of Zao Volcano is the source of the Togatta debris avalanche deposit.

For comparison, the compositions of Minami Zao Volcano are also plotted in Figure 6. Minami Zao Volcano is located south of Zao Volcano. In the northern part of Minami Zao Volcano, a depression can be observed (Figure 2a), which can be interpreted as an erosional caldera or edifice collapse caldera by a phreatic eruption [26]. To further examine this, the whole-rock compositions of the rocks composing the caldera area are plotted in Figure 6. All rocks belong to the medium-K calc-alkaline series, and no tholeiitic series rocks are present. Since the clasts in the Togatta debris avalanche deposit include low-K tholeiitic rocks that are absent from Minami Zao Volcano but present in the Zao volcanic edifice, the petrographic evidence further suggests that the depression at Minami Zao Volcano is unlikely to have been the source. Therefore, this area is unlikely to have been the source of the Togatta debris avalanche deposit, although the genesis of the depression remains unresolved.

4.2. The Volume of the Togatta Debris Avalanche Deposit

The estimated remnant volume of the Togatta debris avalanche deposit is approximately 0.2 km^3. Assuming that roughly one-third of the original volume was lost, mainly due to river erosion, the initial volume is estimated to be about 0.3 km^3. This estimate is based on the observation that the area enclosed by the high-level terraces along the Nigori/Matsukawa Rivers is approximately one-third of the area of the terraces themselves (Figure 2a). This volume is comparable to that of the

 doi:10.20944/preprints202604.0487.v1

Umanose caldera depression, which has been estimated at approximately 0.3 km³, assuming a cylindrical shape with the maximum height taken as the average elevation of the top of the caldera wall, and the base as the near-average elevation of the exposed older products of the Zao Volcano inner caldera.

Reported volumes of volcanic debris avalanche deposits vary widely, depending on the dataset considered. In Japan, [31] examined 71 cases and reported volumes ranging from 0.03 to 9 km³, with a median of approximately 1 km³ for those events with available estimates. [32] later compiled 128 Japanese cases and found that the median volume of the 39 events with quantified estimates is approximately 0.5 km³. [33] examined 58 examples, and based on the diagrams in [33], the median volume is estimated at approximately 0.12–0.15 km³. Globally, among the 50 subaerial volcanic landslides compiled by [34], the median volume is about 0.8 km³. In contrast, more recent historical events (≥0.01 km³ since 1500 CE) compiled by [35] show a median of roughly 0.15 km³, reflecting the predominance of smaller, well-documented modern events.

The estimated initial volume of ~0.3 km³ for the Togatta debris avalanche deposit therefore falls within the small-to-medium range of Japanese Quaternary volcanic examples and is close to the median of global compilations.

4.3. The Mobility of the Togatta Debris Avalanche Deposit

The mobility of a debris avalanche can be assessed using the ratio of vertical drop-to-runout distance of the deposit. The maximum distribution distance of the deposit is 15 km in a straight line from the summit crater, but when measured along the present river course, it is approximately 18 km. The H/L (fall height versus runout distance) relationships compiled for volcanic and non-volcanic debris avalanches demonstrate that volcanic cases systematically exhibit lower H/L values (i.e., higher mobility) than non-volcanic ones (Japanese volcanoes: e.g., [31,32]; global compilations: e.g., [8,34,36]).

For the Togatta debris avalanche deposit, Hmax is calculated from the highest elevation of the caldera rim (1,810 m) and the elevation at the distal end of the deposit (240 m), yielding an Hmax of 1,570 m. Because the flow distance along the present river channel is approximately 18 km, the resulting Hmax/Lmax is 0.09. These data are plotted in the Hmax–Lmax diagram (Figure 9).

The Togatta debris avalanche deposit plots within the lower H/L range among volcanic debris avalanches, indicating relatively high mobility. Although H/L generally shows a negative correlation with volume, the Togatta deposit, despite being small to medium in scale, has an H/L value comparable to those of large-scale debris avalanche deposits.

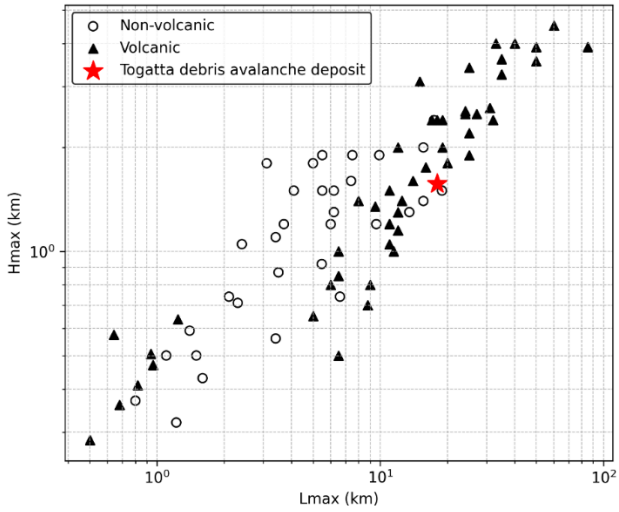

Figure 9. Relationships between total fall height (Hmax), runout distance (Lmax) for subaerial volcanic and subaerial non-volcanic landslides after [34].

 doi:10.20944/preprints202604.0487.v1

4.4. The Age of the Togatta Debris Avalanche Deposit

A calibrated radiocarbon age obtained from the underlying mudstone is approximately 43 ka. This result is generally consistent with previously reported ages for the high terrace (ca. 49–31 cal ka BP based on [18,19]; ca. 42–32 cal ka BP based on [20]). The edifice collapse is considered to mark the onset of the latest activity stage of Zao Volcano, and this study provides additional constraints on the timing of this event.

4.5. The Trigger of the Togatta Debris Avalanche

Edifice collapses rarely result from a single factor; rather, they typically occur through the interaction of preconditioning factors (e.g., steep slopes or weak rocks) and external triggers. Previous studies have identified a variety of processes capable of triggering slope failures in volcanic edifices [9,35,37–39]. For simplicity, these triggers can be broadly classified into three categories: (1) magmatic eruption-related processes, including magma intrusion and eruptive activity; (2) phreatic eruption-related processes, involving increases in subsurface fluid pressure associated with hydrothermal systems, which may lead to phreatic or hydrothermal eruptions; and (3) non-eruptive processes, such as intense rainfall-induced slope instability or strong seismic shaking from large earthquakes.

4.5.1. Possibility of Magmatic or Phreatic Eruption

As described in the Introduction, based on the geomorphological relationships between the caldera and eruptive products distributed around the summit area, the Umanose Caldera is considered to have formed at the onset of the newest stage, although the precise time gap between these eruptions and the caldera collapse remains unclear. The Togatta debris avalanche deposit, however, has only been identified at the foot of the volcano, and its direct stratigraphic relationship with the summit eruptive products remains unclear.

To evaluate whether the Togatta debris avalanche was triggered by an eruption, the stratigraphic relationship between the tephra layers of the newest stage and the Togatta debris avalanche deposit is examined below. Tephra layers of the newest stage are collectively referred to as the Zao-Togatta (Za-To) tephra. The Za-To tephra was originally defined by [11], and the stratigraphic numbering of the layers has subsequently been revised [10,40,41]. The oldest recognized layer is Za-To1.

[20] reported that a tephra layer equivalent to Za-To2 occurs above a conglomerate bed interpreted here as the Togatta debris avalanche deposit, with approximately 1 m of loam intervening between them [42]. The outcrop described in their study is currently covered by vegetation and is no longer observable. Previous studies have shown that a thin loam layer, only a few centimeters thick, is intercalated between Za-To1 and Za-To2, and that Za-To1 is locally absent in some outcrops. Considering these stratigraphic relationships, although Za-To1 was not reported in the outcrop described by [20], it would most likely have been located immediately below Za-To2 if present. Therefore, no tephra layers corresponding to the same or a nearby stratigraphic horizon as the Togatta debris avalanche deposit have been reported, indicating that a direct temporal link between the debris avalanche and eruptive activity remains uncertain.

Previous studies have examined the relationship between the volume of volcanic debris avalanches and their triggering mechanisms. For example, [35] reported that the median volume of eruption-triggered debris avalanches is approximately 0.3 km^3, whereas that of non-eruptive collapses is about 0.05 km^3. The volume of the Togatta debris avalanche examined in this study is estimated at approximately 0.3 km^3. This value is comparable to the median volume of eruption-triggered events reported by [35] and is substantially larger than the typical scale of non-eruptive collapses. These observations suggest that the collapse was most likely associated with eruptive activity.

Distal tephra deposits derived from magmatic eruptions are commonly preserved in the geological record, whereas the tephra layers produced by phreatic eruptions tend to have a more limited dispersal and are less frequently preserved at distal sites [41]. This difference likely reflects

 doi:10.20944/preprints202604.0487.v1

both the relatively small scale of phreatic eruptions and the high moisture content of their ejecta, which promotes deposition near the vent. Although no eruptive deposits directly associated with the debris avalanche have been identified in the study area, this may reflect the relatively distal location of the investigated outcrops. Therefore, a phreatic eruption cannot be completely ruled out as a possible trigger for the debris avalanche.

4.5.2. Possibility of Non-Eruptive Cases

Alternatively, the debris avalanche may have been triggered by non-eruptive processes, such as a large earthquake or intense rainfall. In this scenario, the event would represent an unusually large debris avalanche not directly associated with eruptive activity. Although much of the present Umanose caldera floor is covered by younger volcanic deposits, several areas are thought to preserve remnants of the former caldera floor. Outcrops in these areas commonly exhibit older strata that have undergone hydrothermal alteration (Figure 10). In addition, portions of the caldera wall expose older units that are locally hydrothermally altered. These observations suggest that hydrothermally altered rocks may be widely distributed within the volcanic edifice. Because hydrothermal alteration significantly reduces rock strength, the presence of such weakened zones could have facilitated a relatively large collapse of the summit area even in the absence of a direct eruptive trigger.

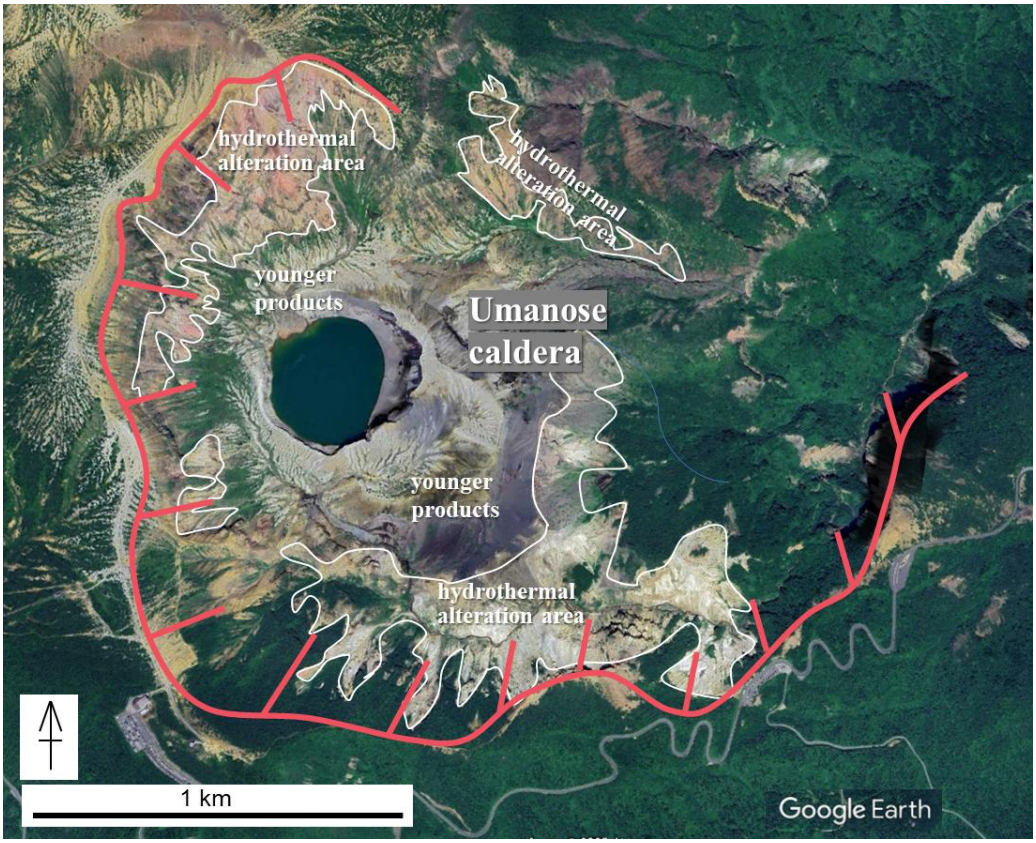

Figure 10. Distribution of the hydrothermal alteration area in the Umanose caldera. The surrounding area of the crater lake Okama is composed of the eruption products younger than the edifice collapse.

4.5.3. Synthesis of Possible Triggering Mechanisms

Taken together, the available evidence suggests that eruptive activity is a plausible trigger for the debris avalanche. The estimated volume of the collapse (~0.3 km^3) is comparable to the median volume of eruption-triggered debris avalanches reported by [35] and is substantially larger than the typical scale of non-eruptive collapses. This relationship and stratigraphic relationships support the interpretation that the collapse was most likely associated with phreatic eruption activity.

 doi:10.20944/preprints202604.0487.v1

However, field observations indicate that hydrothermally altered rocks are locally distributed within the volcanic edifice, particularly in remnants of the former caldera floor and along parts of the caldera wall within the Umanose caldera. Because hydrothermal alteration significantly reduces rock strength, the presence of such weakened zones could have facilitated a large-scale collapse of the summit area even in the absence of a direct eruptive trigger.

Therefore, although an eruption-related origin is consistent with the volume of the debris avalanche, a non-eruptive collapse facilitated by hydrothermal weakening of the volcanic edifice cannot be completely ruled out.

4.6. The Compositional Changes in Eruption Products Across the Caldera Collapse

Changes in magma composition and eruptive style are often linked to variations in the stress state and structural evolution of volcanic edifices. Major edifice or sector collapses can profoundly alter the distribution of mass above magma storage zones, influencing magma reservoir conditions and potentially affecting magma replenishment, pressure, and eruptive behavior (e.g., [43,44]). Numerical modeling and observational evidence indicate that sector collapses may lead to decompression of shallow magma reservoirs and promote the influx of less evolved magma from deeper sources, resulting in changes in erupted magma composition [45,46]. A global synthesis of post--collapse volcanic systems further suggests that deformation and unloading of the volcanic edifice following edifice collapse events can modulate eruptive patterns and the geochemical evolution of magmas, although individual volcanoes exhibit diverse responses (e.g., [43,47]).

At Zao Volcano, the chemical compositions of eruption products from the most recent stage differ markedly from those of the preceding stage associated with the formation of the Umanose caldera [10,24]. For example, a K_2O–SiO_2 diagram for products of the most recent stage (stage 4 by [24]) and the preceding stage (stage 3 by [24]) is shown in Figure 6. The products of the most recent stage are higher in K_2O than those of the preceding stage.

However, magma at Zao Volcano is generally considered to have formed through the mixing of deep and shallow magmas. Therefore, the compositional differences described above are likely attributable to changes in the compositions of both the shallow and deep magmas. Even if gravitational unloading is assumed to be a contributing factor, it is necessary to examine how it may have affected the composition of each magma component. This remains an issue for future study.

5. Conclusions

1. Debris avalanche deposits associated with the collapse of the summit area of Zao Volcano are recognized for the first time at the eastern foot of the volcano. Although dense vegetation in the area generally limits exposure, careful field surveys allowed observation of the deposits at 11 sites. Deposits showing block facies were observed at Locations 1, 2, and 13, while matrix facies dominate at other locations.

2. The deposits extend 11–15 km from the summit, with thicknesses ranging from 20–30 m in the western and northern parts to over 50 m in the eastern part. The estimated initial volume is approximately 0.3 km^3, comparable to the volume of the Umanose caldera depression. The vertical drop-to-runout distance ratio (H/L) is 0.09, which falls within the typical range for volcanic debris avalanches but indicates relatively high mobility.

3. Petrological and geochemical analyses of representative clasts reveal SiO_2 contents ranging from 55–65 wt.%. Based on the petrographic and compositional characteristics, the clasts can be divided into the following four types: (1) medium-K calc-alkaline series two-pyroxene basaltic andesite to dacite, (2) medium-K calc-alkaline series quartz-olivine-bearing two-pyroxene basaltic andesite to andesite, (3) medium-K tholeiitic series quartz-olivine-bearing two-pyroxene basaltic andesite, and (4) low- to medium-K tholeiitic series two-pyroxene basaltic andesite to andesite.

4. Comparison of clast compositions with those of the Zao Volcano edifice indicates that the Togatta debris avalanche deposit originated from the summit Umanose caldera. Apart from a few

 doi:10.20944/preprints202604.0487.v1

medium-K tholeiitic clasts, which are not reported from other volcanoes along the northeast Japan arc, the rock types of the clasts correspond closely to those of the volcanic edifice.

5. The calibrated radiocarbon age of ~43 ka from the underlying mudstone is consistent with previously reported related age estimates.

6. While the collapse was most likely triggered by the phreatic eruption activity, hydrothermally altered rocks within the edifice—especially remnants of the caldera floor and sections of the caldera wall—may have facilitated a large-scale summit collapse even in the absence of direct eruptive activity. Therefore, a non-eruptive collapse mechanism cannot be completely ruled out.

7. Observed changes in magma composition at Zao Volcano are likely related to variations in the relative contributions of deep and shallow magma components. The potential influence of gravitational unloading due to summit collapse on magma composition remains a subject for future study.

Author Contributions: Conceptualization, M.B. and F.O.; methodology, M.B. and F.O.; software, M.B. and F.O.; validation, M.B., F.O., M.S. and T.I.; formal analysis, M.B and F.O..; investigation, M.B., F.O., M.S. and T.I.; resources, F.O. and M.B.; data curation, M.B. and F.O.; writing—original draft preparation, M.B. and F.O.; writing—review and editing, M.B., F.O., M.S. and T.I.; visualization, M.B.; supervision, M.B.; project administration, M.B.; funding acquisition, M.B. All authors have read and approved the final version of the manuscript.

Funding: Please add: This work was supported by MEXT "Integrated Program for Next Generation Volcano Research.".

Data Availability Statement: All data presented in this study are included in this article.

Acknowledgments: We are especially grateful to Mr. Tomiya Murakami and Ms. Kirika Kitagawa of the Zao Town Geopark Promotion Office, Miyagi Prefecture, for their assistance in obtaining permission to conduct research on private land in the town, and we also thank the other staff members for their support.

Conflicts of Interest: The authors declare no conflict of interest.

References

1. Voight, B.; Glicken, H.; Janda, R.J.; Douglass, P.M. Rockslide-debris avalanche at Mount St. Helens, Washington. *Nature* **1983**, 304, 242–244.
2. Christiansen, R.L.; Peterson, D.W. Chronology of the 1980 eruptive activity. In *The 1980 eruptions of Mount St Helens, Washington*; Lipman, P.W., Mullineaux, D.R., Eds.; US Geol Surv. Prof. Paper, 1981; 1250, pp. 17-30.
3. Nakamura, Y.; Glicken, H. Blast and debris-avalanche deposits of the 1888 eruption Bandai volcano. *J. Geogr. (Chigaku Zasshi)* **1988**, 97, 309–316, (In Japanese with English abstract).
4. Ui, T. Pyroclastic flows and eruptions at Mount Bandai, Japan. *J. Volcanol. Geotherm. Res.* **1983**, 18, 135–150.
5. Yamamoto, T.; Nakamura, Y.; Glicken, H. Pyroclastic density current from the 1888 phreatic eruption of Bandai volcano, NE Japan. *J. Volcanol. Geotherm. Res.* **1999**, 90, 191–207.
6. Siebert, L. Large volcanic debris avalanches: Characteristics of source areas, deposits, and associated eruptions. *J. Volcanol. Geotherm. Res.* **1984**, 22, 163–197.
7. Siebert, L. Hazards of Large Volcanic Debris Avalanches and Associated Eruptive Phenomena. In *Monitoring and Mitigation of Volcano Hazards*; Lipman, P.W., Mullineaux, D.R., Eds.; Springer: Germany, 1996; pp. 541–572.
8. Dufresne, A.; Siebert, L.; Bernard, B. 2021. Distribution and Geometric Parameters of Volcanic Debris Avalanche Deposits. In *Volcanic debris avalanches*; Roverato, M., Dufresne, A., Procter, J. Eds.; Adv. Volcanol., 2021, 6, pp. 75-90.
9. van Wyk de Vries, B. Landslides, debris avalanches, and volcanic gravitational deformation. In *Encyclopedia of Volcanoes*, 2nd ed.; Sigurdsson, H., Houghton, B., McNutt, S.R., Rymer, H., Stix, J. Siebert, K., Eds.; Academic Press, 2015; pp. 665–685.

 doi:10.20944/preprints202604.0487.v1

10. Ban, M.; Oikawa, N.; Yamazaki, S. Geological Map of Zao Volcano; *Geological Map of Volcanoes, no 18*; Geological Survey of Japan, AIST: Tsukuba, Japan, 2015.
11. Imura, R. Eruption history of Goshikidake, Zao Volcano. In *abstr. 1994 Autumn Meet. Volcanol. Soc. Japan*, 1994, 92, (In Japanese).
12. Reimer, P.J.; Austin, W.E.N.; Bard, E.; Bayliss, A.; Blackwell, P.G.; Bronk Ramsey, C.; Butzin, M.; Cheng, H.; Edwards, R.L.; Friedrich, M.; Grootes, P.M.; Guilderson, T.P.; Hajdas, I.; Heaton, T.J.; Hogg, A.G.; Hughen, K.A.; Kromer, B.; Manning, S.W.; Muscheler, R.; Palmer, J.G.; Pearson, C.; van der Plicht, J.; Reimer, R.W.; Richards, D.A.; Scott, E.M.; Southon, J.R.; Turney, C.S.M.; Wacker, L.; Adolphi, F.; Büntgen, U.; Capano, M.; Fahrni, S.M.; Fogtmann--Schulz, A.; Friedrich, R., Köhler, P.; Kudsk, S.; Miyake, F.; Olsen, J.; Reinig, F.; Sakamoto, M.; Sookdeo, A.; Talamo, S. The IntCal20 Northern Hemisphere radiocarbon age calibration curve (0–55 cal kBP). *Radiocarbon* **2020**, 62, 725–757.
13. Yamada, Y.; Kohno, H.; Murata, M. A low dilution fusion method for major and trace element analysis of geological samples. *Advan. X-ray Anal.* **1995**, 26, 33–44, (In Japanese with English abstract).
14. Ban, M.; Takahashi, K.; Horie, T.; Yoya, N. Petrogenesis of mafic inclusions in rhyolitic lavas from Narugo Volcano, Northeastern Japan. *J. Petrol.* **2005**, 46, 1543–1563.
15. Matsui, K.; Abe, M.; Inoue, T.; Masago, S.; Ishino, K.; Oide, K.; Nakagawa, H.; Shoji, M.; Kaneko, S.; Ando, Y.; Ishida, T.; Takahashi, H.; Akama, Y. *Geological survey report of the Zao Volcano foot area.* Tohoku Regional Agricultural Administration Bureau, Planning Department, Eds.; Tohoku Regional Agricultural Administration Bureau: Japan, 1971; pp. 21–48, (In Japanese).
16. Tayama, R. Geomorphological study of river terraces near Sendai. *Saito Hōonkai Sci. Rep* **1933**, 17, 1–83, (In Japanese).
17. Nakagawa, H.; Ogawa, S.; Suzuki, Y. Quaternary geology and geomorphology near Sendai. *Quaternary Res.* **1960**, 1, 219–227, (In Japanese with English abstract).
18. Takeuchi, S. Pollen analysis of low terraces near Sendai. In *Prof. Nobu Kitamura Mem. Geol. Papers*; Nakagawa, H. et. al., Eds.; Commemorative Society for Professor Nobu Kitamura's Retirement: Sendai, Japan, 1986: 517–526, (In Japanese).
19. Takeuchi, S. ^{14}C dating of Sendai Kamimachi terrace deposits. *Chikyu Kagaku* **1986**, 40, 301–302, (In Japanese with English abstract).
20. Itagaki, N.; Toyoshima, M.; Terado, T. Holocene scoria layers in Sendai and surrounding areas. *Tohoku Geogr.* **1981**, 33, 48–53, (In Japanese)
21. Glicken, H. Rockslide-debris avalanche of May 18, Mount St. Helens Volcano, Washington. *USGS Open-file Report* 1996, 96-677, pp. 1–90.
22. Sánchez-Núñez, J.M.; Macías, J.L.; Arce, J.L.; Gómez, J.C. The Chuquibamba Landslide Western Cordillera, Peru revisited: New evidence of a dry debris avalanche, **2025**, 64-1, 48–53.
23. Kitamura, N.; Nakagawa, H. *Basic land classification 1:50,000 "Shiroishi": Surficial geology map and explanatory notes*; Miyagi Prefecture: Sendai, Japan, 1983; pp. 25–36.
24. Sakayori, A. Geology and petrology of Zao Volcano. *J. Japanese. Assoc. Mineral. Petrol. Econ. Geol.* **1992**, 87, 433-444, (In Japanese with English abstract).
25. Tatsumi, Y.; Takahashi, T.; Hirahara, Y.; Chang, Q.; Miyazaki, T.; Kimura, J. I.; Ban, M.; Sakayori, A. New insights into andesite genesis: the role of mantle-derived calc-alkalic and crust-derived tholeiitic melts in magma differentiation beneath Zao Volcano, NE Japan. *Journal of Petrology* **2008**, 49, 1971-2008.
26. Sakayori, A. Geology of Minami Zao volcano. *J. Japanese. Assoc. Mineral. Petrol. Econ. Geol.* **1985**, 80, 94-103, (In Japanese with English abstract).
27. Gill, J.B. Orogenic Andesites and Plate Tectonics; Springer: Berlin/Heidelberg, Germany; New York, NY, USA, 1981; pp. 1–392.
28. Miyashiro, A. Volcanic rock series in island arcs and active continental margins. *Am. J. Sci.* **1974**, 274, 321–355.
29. Sakuyama, M. Evidence of magma mixing: petrological study of Shirouma-Oike calc-alkaline andesite volcano, Japan. *J. Volcanol. Geotherm. Res.* **1979**, 5, 179–208.

 doi:10.20944/preprints202604.0487.v1

30. Ban, M.; Kimura, J.-I.; Takahashi, T.; Hirahara, Y.; Ohba, T.; Fujinawa, A.; Hayashi, S.; Yoshida, T.; Miyazaki, T.; Tsuchiya, N.; Kagashima, S.-I.; Chang, Q.; Senda, R.; Vaglarov, B. S.; Tatsumi, Y. The significant role of the mafic lower crust in the chemical diversity of arc magmas. *Island Arc* **2025**, 34, e70033.
31. Ui, T.; Yamamoto, H.; Suzuki-Kamata, K. Characterization of debris avalanche deposits in Japan. *J. Volcanol. Geotherm. Res.* **1986**, 29, 231–243.
32. Inokuchi, T. Properties of sector-collapse and debris avalanche on quaternary volcanoes in Japan. *J. Jpn. Landslide Soc.* **2006**, 42, 409–420, (In Japanese with English abstract).
33. Yoshida, H. Catastrophic Sector Collapses of Quaternary Volcanoes as Significant Sediment Sources in Japan. *J. Geogr. (Chigaku Zasshi)* **2010**, 119, 568–578, (In Japanese with English abstract).
34. Legros, F. The mobility of long-runout landslides. *Eng. Geol.* **2002**, 63, 301–331.
35. Siebert, L.; Reid, M.E.. Lateral edifice collapse and volcanic debris avalanches: a post--1980 Mount St. Helens perspective. *Bull. Volcanol.* **2023**, 85:61.
36. Scheidegger, A. On the prediction of the reach and velocity of catastrophic landslides. *Rock Mechanics* **1973**, 5, 231–236.
37. Siebert, L.; Glicken, H.; Ui, T. Volcanic hazards from Bezymianny- and Bandai-type eruptions. *Bull. Volcanol.* **1987**, 49, 435–459.
38. McGuire, W.J. Volcano instability: a review of contemporary themes. *Geological Society, London, Special Publications* **1996**, 110, 1–23.
39. Ui, T.; Takarada, S.; Yoshimoto, M. Debris avalanches avalanches. In *Encyclopedia of Volcanoes*; Tobin, H., Witter, C. Eds.; Academic Press, 2000; pp. 617–626.
40. Ban, M.; Sagawa, H.; Miura, K.; Hirotani, S. Evidence for a short--lived stratified magma chamber: petrology of the Za--To tephra layer (~5.8 ka) at Zao volcano, NE Japan. In *Dynamics of Crustal Magma Transfer, Storage, and Differentiation*; G. Zellmer, G., Annen, C., Eds.; Geological Society, London, Special Publications, 304, 2008, pp. 149–168.
41. Ban, M.; Oikawa, T.; Imura, T.; Tsunematsu, K.; Jin, H.; Takahashi, Y. An Example of the Magma Discharge Step-diagram: Zao Volcano. In *Magma Discharge Step-diagrams of Japanese Active Volcanoes*; Technical Note of the National Research Institute for Earth Science and Disaster Resilience 2023, 500, pp. 37–43 (In Japanese with English abstract).
42. Miura, K., Ban, M. and Yagi, K., 2008, The tephra layers distributed around the eastern foot of the Zao volcano -Ages and volumes of the Za-To 1 to 4 tephras-. *Bull. Volcanol. Soc. Japan*, **53**, 151–157.
43. Manconi, A.; Bagnardi, M.; Tait, S.; Walter, T.R. Sector collapses and magmatic system response at ocean island volcanoes. *J. Volcanol. Geotherm. Res.* **2009**, 182, 85–100.
44. Boudon, G.; Villemant, B.; Le Friant, A.; Paterne, M.; Cortijo, E. Role of large flank-collapse events on magma evolution of volcanoes: Insights from the Lesser Antilles Arc. *J. Volcanol. Geotherm. Res.* **2013**, 263, 224–237.
45. Longpré, M.-A.; Troll, V.R.; Walter, T.R.; Hansteen, T.H. Volcanic and geochemical evolution of the Teno massif, Tenerife, Canary Islands: Some repercussions of giant landslides on ocean island magmatism. *Geochemistry, Geophysics, Geosystems* **2009**, 10(12), Q12017.
46. Pinel, V.; Albino, F. Consequences of volcano sector collapse on magmatic storage zones: Insights from numerical modeling. J. Volcanol. Geotherm. Res. 2013, 252, 29–37.
47. Wat, S.F.L. The evolution of volcanic systems following sector collapse. *J. Volcanol. Geotherm. Res.* **2019**, 384, 280–303.